Cross-Scale Coefficient Selection for Volumetric Medical Image Fusion

Rui Shen, *Student Member, IEEE,* Irene Cheng, *Senior Member, IEEE,* and Anup Basu, *Senior Member, IEEE*

***Abstract*—Joint analysis of medical data collected from different imaging modalities has become a common clinical practice. Therefore, image fusion techniques, which provide an efficient way in combining and enhancing information, has drawn increasing attention from the medical community. In this paper, we propose a novel cross-scale fusion rule for multiscale decomposition (MSD)-based fusion of volumetric medical images taking into account both intra- and inter-scale consistencies. Instead of employing computationally expensive MSD schemes to improve fusion results, our cross-scale fusion rule determines an optimal set of coefficients from the multiscale representations of the source images by effective exploitation of neighborhood information. An efficient color fusion scheme is also proposed. Experiments demonstrate that our fusion rule generates better results than existing rules.**

***Index Terms*—Medical image fusion, 3D image fusion, fusion rule, multiscale analysis.**

I. Introduction

MEDICAL imaging has become a vital component in routine clinical applications, such as diagnosis and treatment planning [1]. However, because each imaging modality only provides information in a limited domain, many studies require joint analysis of imaging data collected from the same patient using different modalities [2]. For instance, T_1-weighted (T1W) and T_2-weighted (T2W) magnetic resonance imaging (MRI) brain scans were analyzed together to guide neurosurgical resection of epileptogenic lesions [3] or to identify thalamic nuclei [4]; MRI and computed tomography (CT) images were analyzed together to judge the quality of a prostate seed implant [5]; and MRI and poitron emission tomography scans were analyzed together to diagnose intracranial tumors [6]. This requirement of joint analysis of multi-modal imaging data led to the introduction of image fusion techniques into the medical field and the development of medical data-oriented fusion techniques (*e.g.,* [7], [8]). Given a set of source images, image fusion not only provides a single fused image with more accurate and reliable information than any individual source image, but may also enable features to be more distinguishable in the fused image [9]. Such an enhanced image facilitates visual perception or further image processing tasks [10], [11]. Due to its compact and enhanced representation of information, image fusion has been employed in many medical applications, such as tumor detection and diagnosis, neurosurgical monitoring and planning [12], and quality enhancement of four-dimensional (4D) fetal cardiac ultrasound imaging [8]. Even if image fusion is not performed explicitly, *e.g.,* by a computer program, it is common practice for radiologists to utilize complementary information obtained by different imaging modalities [1], [2], [13], and the fusion of information from multi-modality medical images is usually performed subconsciously by radiologists to compare images and better identify abnormality [13].

R. Shen, I. Cheng, and A. Basu are with the Department of Computing Science, University of Alberta, Edmonton, AB, T6G 2E8 Canada (e-mail: rshen@ualberta.ca; locheng@ualberta.ca; basu@ualberta.ca).

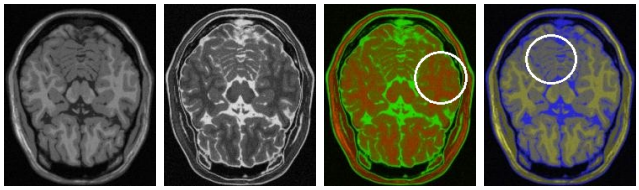

(a) (b) (c) (d)

Fig. 1. Overlaying monochrome images using different color channels. The overlaying schemes transfer information from both T1W and T2W MRI images into a single image at the cost of reduced image contrast. (a) T1W MRI image; (b) T2W MRI image; (c) Overlaid image using the red channel for T_1 and the green channel for T_2; (d) Overlaid image using the red and green channels for T_1 and the blue channel for T_2.

In some medical practice, image fusion is achieved by overlaying co-registered images acquired from different modalities [14] or overlaying regions of interest (ROIs) or features extracted from one modality with images captured from another [3]. Normally, the co-registered source images or ROIs are overlaid by manipulating their transparency attributes (if a source image contains color information) [13] or assigning them to different color planes (if the sources are monochrome/grayscale images) [15]. This practice is considered as a fundamental approach in color fusion, where the use of color expands the amount of information that can be conveyed in a single image [16]. While such overlaying schemes aim to transfer information visually from multiple sources to a single displayed image (not physically blending the pixel values to form a new image), they do not necessarily enhance the image contrast or make image features more distinguishable. An example is given in Figure 1, where the overlaying schemes transfer information from both T1W and T2W MRI scans into a single image at the cost of reduced image contrast (compare the regions indicated by the white circles between the overlaid images and the original images). In our study, we treat image fusion as the process of physically blending the pixel values stored in the source images, which is a common interpretation in the image fusion community for monochrome image fusion [10], [16]. In addition, we also show how color fusion can benefit from the monochrome fusion results.

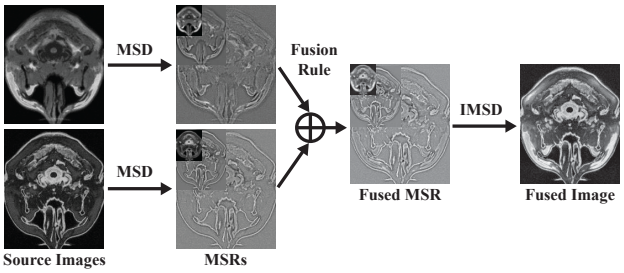

Fig. 2. General procedure of MSD-based image fusion in a 2D case.

According to whether multiscale decomposition (MSD) (*e.g.,* pyramid transform) is used, fusion methods can be classified into two categories: MSD-based and non-MSD based. Compared to the latter, MSD-based methods have the advantage of extracting and combining salient features at different scales, and therefore normally produce images with greater information content [16]. The general procedure of MSD-based fusion in a 2D case is illustrated in Figure 2. First, the source images are transformed to multiscale representations (MSRs) using MSD. An MSR is a pyramidal structure with successively reduced spatial resolution; and it usually has one approximation level storing low-pass coefficients and several detail levels storing high-pass or band-pass coefficients. Then, a certain fusion rule is applied to merge coefficients at different scales. Finally, an inverse MSD (IMSD) is applied to the fused MSR to generate the final image.

According to [9], [16]–[18], image fusion can be performed at three different levels: pixel/data level, feature/attribute level, and symbol/decision level. Pixel-level fusion determines a pixel in the fused image from a set of pixels in the source images. Feature-level fusion applies the extracted image features (*e.g.,* segmented objects or edge maps) to guide the pixel merging process or form a joint feature vector. Symbol-level fusion combines abstract representations of the source images extracted using techniques like classification. Among these three levels, pixel-level fusion and feature-level fusion are more closely related when both output a single fused image, while the output of symbol-level fusion is always a certain decision. Pixel-level fusion directly uses the original information in the source images and is computationally efficient, but it is more sensitive to image noise compared to feature-level fusion [18]. However, the fusion quality of feature-level methods largely depends on the performance of the employed feature extraction technique. In practice, a fusion task may also involve more than one level simultaneously [17], [18].

In this paper, we propose a novel cross-scale (CS) fusion rule for MSD-based image fusion, where the belongingness/membership of each fused coefficient to each source image is calculated. Although here we focus on pixel-level fusion, this proposed fusion rule can be extended to feature-level or symbol-level fusion as well. Unlike previous methods, our fusion rule calculates an optimal set of coefficients for each scale taking into account large neighborhood information, which guarantees intra- and inter-scale consistencies. The effectiveness of this new fusion rule is validated through experiments on 3D medical image fusion. Although it is possible to treat 3D images/volumes as stacks of 2D slices and fuse corresponding slices using 2D fusion methods, the results do not have qualities comparable to 3D fusion due to lack of between-slice information in the fusion process [19]. Therefore, in our method, we apply MSD and our CS rule directly to the 3D volumes. An effective color fusion scheme utilizing the monochrome fusion results is also proposed.

The rest of the paper is organized as follows. Section II reviews previous methods. Section III explains our cross-scale fusion rule and our color fusion scheme in detail. Section IV discusses experimental results, along with comparison with existing fusion rules. Finally, Section V gives the conclusion and future work.

II. Related Work

This section focuses on reviewing key MSD-based image fusion techniques. For applications of image fusion in medicine and other fields, please refer to the overview articles by Pattichis *et al.* [12] and by Hall and Llinas [20].

A. Multiscale Decomposition

The pyramid transform (PT) and the wavelet transform (WT) are the two categories of MSD schemes that are most commonly employed in image fusion. Among different PT schemes, the Laplacian pyramid transform (LPT) [21], [22] is one of the most frequently used in image fusion. A Laplacian pyramid (LP) is constructed based on its corresponding Gaussian pyramid by subtracting two adjacent levels. Thus, a detail level in the LP encodes the local variations at that scale. The ratio of low-pass pyramid (RoLP) [23] is also constructed based on the Gaussian pyramid, but by taking the ratio of two adjacent levels. When an RoLP is used in subsequent calculations, the local contrast (*i.e.,* local luminance variation with respect to the background [24]) at each coefficient location in the RoLP is derived from the ratio. The gradient pyramid (either explicitly [25] or implicitly [26] constructed) is another type of PT, which is built by applying gradient filters of different orientations to each level of a Gaussian pyramid.

Other than PT, WT introduced by Mallat [27] has also been successfully applied to image fusion (*e.g.,* [28], [29]). A standard WT technique is the discrete WT (DWT) [27], which decomposes a signal into an MSR using scaling (low-pass filtering) and wavelet (high-pass filtering) functions. One drawback of DWT is shift-variance, which tends to cause artifacts along edges in the fused images [29], [30]. To solve this problem in DWT-based fusion, WT schemes that provide shift-invariance, such as redundant DWT [31] and dual-tree complex WT (DT-CWT) [32], were also employed in image fusion. Please refer to [30] for detailed discussions on the performance of different MSD schemes in some representative fusion tasks. Instead of employing sophisticated MSD schemes to improve the fusion stability, which usually dramatically increase the computational cost, here we focus on the other direction to provide stable fusion results, *i.e.,* utilizing more effective fusion rules.

Although theoretically the decomposition of an image can be performed iteratively until there is only one pixel in each dimension at the approximation level, this will result in serious bias and inaccuracy in the feature selection at low-resolution levels, which impairs the fusion quality [26]. Therefore, typically only a few decomposition levels are used in practice, and some analyses on the number of decomposition levels for different MSD schemes in some fusion tasks were conducted in [30], [33].

B. Fusion Rules

Other than the MSD scheme, the other key factor affecting the fusion results is the fusion rule. According to [9], [11], a fusion rule is the processing that determines the formation of the fused MSR from the MSRs of the source images, and it consists of four key components, *i.e.,* activity-level measurement, coefficient grouping, coefficient combining, and consistency verification. In this section, we give a brief review of some representative schemes in these four steps. Please refer to [9], [11], [33] for more detailed discussions.

1) Activity-Level Measurement: The activity-level measurement reflects the salience of each coefficient in an MSR [30], and it can be categorized into three classes, *i.e.,* coefficient-based activity (CBA), window-based activity (WBA), and region-based activity (RBA) [9], [11]. A CBA measure evaluates each coefficient independently and normally describes the activity level of a coefficient using its absolute value. A WBA measure uses the information within a window to evaluate the coefficient at the window center. A popular choice is the rank filter-based WBA, where the maximum value within a window is normally selected as in [28]. More sophisticated WBA measures also exist in the literature, such as image statistics-based WBA [33]. The concept of RBA is similar to WBA except that irregular-shaped regions are used instead of regular-shaped windows. RBA is one way to achieve feature-level fusion, which requires segmentation on (the MSRs of) the source images [18], [34]. In our CS rule, the activity-level measure is used to determine the salience at each coefficient and there is no restriction on the type of measures to be employed. The focus of our CS rule is to provide a unified framework of the other three key components in a fusion rule, which are usually treated separately in previous methods.

2) Coefficient Grouping: The coefficient grouping schemes can be roughly divided into three categories, *i.e.,* no grouping (NG), single-scale grouping (SG), and multiscale grouping (MG) [9], [11]. NG means that each coefficient is fused independently; SG means that corresponding coefficients between different subbands at the same decomposition level are fused in the same way; and MG is more restrictive than SG by also requiring that corresponding coefficients between different scales take the same fusion decision. For some types of PT, *e.g.,* LPT and RoLP, where only one subband is present at each decomposition level, NG and SG are equivalent. A cross-band SG (CBSG) scheme was proposed in [35], where the same fusion decision for every set of corresponding detail coefficients at the current scale is made based on the sum of the activity levels of them and their corresponding coefficients at a higher scale. An MG scheme was proposed in [36], where the fusion decision for every set of corresponding coefficients across all scales in an MSR is made based on the weighted average of their activity levels. Our CS rule performs similar to MG, but does not impose such a hard constraint on the fusion decision. Instead, the influence on each coefficient from their corresponding coefficients at adjacent scales is reflected in the membership calculation, and the fusion decision of a coefficient is determined based on its calculated membership. Please refer to Section III for a detailed description on the membership calculation.

3) Coefficient Combining: One common coefficient combining scheme for the detail levels is the choose-max (CM) combining scheme, *i.e.,* selecting the coefficient with the highest activity level at each location from the MSRs of the source images as the coefficient at that location in the MSR of the fused image [9]. A common combining scheme for the approximation level is taking average (AVG). Another popular scheme for the approximation level is the weighted average (WA) combining scheme proposed in [25]. A linear weighting function is applied when the local correlation between corresponding coefficients in a neighborhood in the MSRs of the source images is above a threshold. Some more complicated combining schemes were also proposed by previous researchers, and please refer to [33] for more detailed discussions. Our CS rule does not apply combining schemes directly based on coefficient activity levels, but combines coefficients based on their memberships, which results in a more effective combining scheme utilizing inter- and intra-scale information.

4) Consistency Verification: The consistency verification schemes ensure neighboring coefficients are fused in a similar manner [9]. A majority filter was used in [28] to apply window-based verification (WBV) at each individual scale. A cross-band verification (CBV) scheme was proposed in [35], where the detail coefficients at the current level of the fused MSR are recalculated if their corresponding coefficients at a lower level come from the MSR of a different source image. CBV was designed to comply with CBSG. It is also possible that no verification (NV) is applied. Our CS rule does not perform explicit verification, but embeds verification in the coefficient membership calculation process.

C. Medical Image Fusion

The overlaying schemes were discussed in Section I and here we focus on the discussion of fusion techniques that physically blend pixel values in medical images. Please note that the MSD-based fusion methods discussed in the previous sections can be directly applied to multi-dimensional medical image fusion, such as the DWT+CBA+NG+AVG+CM+NV method used in [37] for quality enhancement of real-time 3D echocardiography. In this section, we discuss some activity-level measures proposed by previous researchers for medical image fusion and some non-MSD based methods. A multi-channel pulse coupled neural network was proposed in [38] for 2D medical image fusion. However, the fusion results suffer from loss of local contrast, which makes details less

distinguishable. DWT was applied to fuse 2D medical images in [39], where a visibility-based WBA and a local variance-based WBA were proposed for the approximation level and the detail levels, respectively. NG, CM for both the approximation and detail levels, and WBV were employed. However, no experiment specifically designed to prove the advantages of their proposed WBA measures compared to other activity-level measures was conducted. In contrast, all fusion rules were compared under the same setting in our experiments, *i.e.,* using the same MSD scheme and activity-level measure.

In [19], 3D shunting neural network was applied for information decorrelation between source images and the shunted images were then assigned to different color planes for color fusion of 3D medical images. In our method, a more efficient scheme is proposed, where color fusion is achieved as a natural extension to monochrome fusion. In addition, our method is developed based on the color opponency theory [40], which maximizes color contrast. A multi-band contrast field defined on image gradients was proposed in [41] and the fused 3D medical image was obtained by minimizing a quadratic objective function defined using the contrast field. Please note that the contrast definition used in [41] is different from classic definitions [23], [24], where contrast is defined as luminance variation with respect to background luminance. As mentioned in [41], their method tends to cause artifacts in smooth image regions due to the form of the objective function. Such artifacts are less likely to appear in our method, because the fused voxel values are closely related to the source voxel values and both intra- and inter-scale consistencies are imposed. In addition, our focus here is a novel fusion rule other than a specific activity-level measure (*e.g.,* contrast) and different measures can be easily incorporated into our fusion rule.

III. Method

A. Problem Formulation

The source images are assumed to be spatially registered, which is a common assumption in image fusion [9]–[11]. Various techniques can be applied to medical image registration. Please refer to the excellent surveys by Maintz and Viergever [1] and by Shams *et al.* [42] for more details. Let $c^n_{k,d,i}$ and $\bar{c}^n_{d,i}$ denote the i-th coefficients in the d-th subband at the n-th detail level of the MSR of the k-th source image and the fused image, respectively, where $n \in [1, N]$. Let $a_{k,d,i}$ and $\bar{a}_{d,i}$ denote the i-th coefficients in the d-th subband at the approximation level of the MSR of the k-th source image and the fused image, respectively. We assume a subband at the approximation level has the same size as a subband at the N-th detail level. For PT schemes where the approximation level is at a higher level, applying an extra step of band-pass filtering can fulfill this assumption. Let $M : \{\bar{c}^n_{d,i}, \bar{a}_{d,i}\} \times \{c^n_{k,d,i}, a_{k,d,i}\} \to [0, 1]$ be a function representing the (partial) membership of $\bar{c}^n_{d,i}$ (or $\bar{a}_{d,i}$) to the MSR of the k-th source image, *i.e.,* the proportion of the contribution from $c^n_{k,d,i}$ (or $a_{k,d,i}$) to $\bar{c}^n_{d,i}$ (or $\bar{a}_{d,i}$) among all corresponding coefficients $\{c^n_{k,d,i} | k = 1, \ldots, K\}$ (or $\{a_{k,d,i} | k = 1, \ldots, K\}$). The memberships can be determined based on local and/or global information in the MSRs. To simplify notation, let $M^n_{k,d,i}$ and $M_{k,d,i}$ denote the coefficient memberships at the n-th detail level and the approximation level, respectively. We have $\sum_k M^n_{k,d,i} = 1$ and $\sum_k M_{k,d,i} = 1$.

For each subband of a detail level, where the corresponding coefficients among different MSRs are usually quite distinct from each other, a fused coefficient can be determined as the one with the highest membership:

$$\bar{c}^n_{d,i} = \arg\max_{c^n_{k,d,i}, k:1\ldots K} M^n_{k,d,i}. \tag{1}$$

For the approximation level, where the corresponding coefficients usually exhibit less diversity compared to those at a detail level, a fused coefficient can be determined as a weighted average of all its corresponding coefficients based on their memberships:

$$\bar{a}_{d,i} = \sum_{k=1}^{K} M_{k,d,i} a_{k,d,i}. \tag{2}$$

B. Cross-Scale Coefficient Selection

The proposed cross-scale fusion rule aims to pass information within and between each decomposition level so that the fused image preserves most details from the source images while exhibiting minimal artifacts. The basic steps are: 1) Pass salient information from a lower level to a higher level in an MSR until the approximation level is reached; 2) Calculate the memberships of each fused coefficient at the approximation level using the passed salient information; 3) Use these memberships to guide the coefficient selection at the detail levels.

Let $A^n_{k,d,i}$ denote the activity level of $c^n_{k,d,i}$. In order to impose inter-scale consistency, the activity levels of coefficients at a lower decomposition level are passed to a higher level as follows:

$$\tilde{A}^n_{k,d,i} = \begin{cases} \mathrm{erf}(A^n_{k,d,i}), & n = 1; \\ \max(\mathrm{erf}(A^n_{k,d,i}), [\tilde{\mathbf{A}}^{n-1}_{k,d}]^{\downarrow 2}_i), & n \in [2, N]. \end{cases} \tag{3}$$

where $\tilde{\mathbf{A}}^n_{k,d}$ denotes the vector containing all $\tilde{A}^n_{k,d,i}$'s in the d-th subband of the MSR of the k-th source image; $[\cdot]^{\downarrow 2}$ denotes downsampling by a factor of 2 in each dimension; and the subscript $[\cdot]_i$ denotes the i-th coefficient. $\mathrm{erf} : \mathbb{R} \to [-1, 1]$ is called the Gauss error function, a sigmoid-shaped function. The magnitudes of activity levels of the coefficients across different detail levels can vary significantly, which makes it difficult to compare the relative importance of salient information across scales. This nonlinear function $\mathrm{erf}(\cdot)$ compresses the activity levels into the same range $[0, 1]$, which gives a more reasonable comparison of salient information.

At the approximation level, the passed salient information $\tilde{A}^N_{k,d,i}$'s and the approximation coefficients $a_{k,d,i}$'s are used together to calculate the memberships $M_{d,i,k}$'s. One simple scheme is to directly take normalized $\tilde{A}^N_{k,d,i}$'s as $M_{d,i,k}$'s. However, this scheme does not utilize the visual information embedded in $a_{k,d,i}$'s, which is crucial for producing locally smoothed solutions. The generalized random walks (GRW) proposed in [43] has demonstrated good performance in imposing intra-scale consistency while preserving local details in multi-exposure fusion. Therefore, here we employ

Algorithm 1 Basic steps of the LPT+CS fusion scheme.

1: Apply N-level LPT to each source image
2: Apply band-pass filtering to the approximation levels
3: Compute $\tilde{A}^n_{k,1,i}$'s for detail level 1 to N using Equation (3)
4: Compute $M_{k,1,i}$'s at the approximation level using Equations (4) to (6)
5: Compute $M^n_{k,1,i}$'s for detail level N to 1 using Equation (7)
6: Select coefficients for the approximation level of the fused MSR using Equation (2)
7: Select coefficients for the detail levels of the fused MSR using Equation (1)
8: Apply inverse LPT to the fused MSR

Algorithm 2 Basic steps of the DWT+CS fusion scheme.

1: Apply N-level DWT to each source image
2: Compute $\tilde{A}^n_{k,1,i}$'s for detail level 1 to N using Equations (8) and (3)
3: Compute $M_{k,1,i}$'s at the approximation level using Equations (4) to (6)
4: Compute $M^n_{k,1,i}$'s for detail level N to 1 using Equation (7)
5: Assign $M^n_{k,1,i}$'s to their corresponding $M^n_{k,d,i}$'s
6: Select coefficients for the approximation level of the fused MSR using Equation (2)
7: Select coefficients for the detail levels of the fused MSR using Equation (1)
8: Apply inverse DWT to the fused MSR

GRW to calculate $M_{d,i,k}$'s, which we consider as the steady-state transition probabilities in the random walks context, by minimizing K similarly-defined energy functions. Let $\mathbf{M}_{k,d}$ denote the vector containing all $M_{d,i,k}$'s, *i.e.,* memberships of all the approximation coefficients in the d-th subband of the fused MSR to the k-th source image. The solution to the k-th energy function is given by:

$$\mathbf{L}_d \mathbf{M}_{k,d} = \tilde{\mathbf{A}}^N_{k,d}. \tag{4}$$

The matrix $\mathbf{L}_d$ is called the Laplacian matrix, which encodes the interactions between adjacent coefficients. The entry in the i-th row and j-th column is defined as:

$$\mathbf{L}_{d,ij} = \begin{cases} \sum_{\bar{a}_{d,s} \in \mathcal{N}_{d,i}} W_{d,is} + \sum_k \tilde{A}^N_{k,d,i}, & i = j; \\ -W_{d,ij}, & \bar{a}_{d,j} \in \mathcal{N}_{d,i} \\ 0, & \text{otherwise.} \end{cases} \tag{5}$$

where $\mathcal{N}_{d,i}$ is the first-order neighborhood of $\bar{a}_{d,i}$. $W_{d,ij}$ represents the expected similarity between $\bar{a}_{d,i}$ and $\bar{a}_{d,j}$ based on the observed approximation coefficients in the MSRs of the source images. $W_{d,ij}$ is defined as follows:

$$W_{d,ij} = \gamma \prod_{k=1}^{K} \exp\left(\frac{\|a_{k,d,i} - a_{k,d,j}\|}{\sigma}\right), \tag{6}$$

where γ and σ are weighting factors. Please refer to [43] for more details on GRW.

Once $M_{d,i,k}$'s are calculated, they are passed down to guide the membership calculation at each detail level:

$$M^n_{k,d,i} = \begin{cases} M_{d,i,k}, & n = N; \\ \frac{1}{\alpha}[\phi * (\tilde{\mathbf{A}}^n_{k,d} \odot [\mathbf{M}^{n+1}_{k,d}]^{\uparrow 2})]_i, & n \in [1, N-1]. \end{cases} \tag{7}$$

where α is a normalization factor rendering $\sum_k M^n_{k,d,i} = 1$; $[\cdot]^{\uparrow 2}$ denotes upsampling by a factor of 2 in each dimension followed by interpolation; $*$ denotes convolution; $\odot$ denotes component-wise multiplication; and ϕ is a low-pass filter that helps to achieve intra-scale consistency. In our current implementation, ϕ is taken as a $5 \times 5 \times 5$ Gaussian filter for a volume. In the following, we give two specific examples on applying our CS rule with two popular MSD schemes, LPT and DWT. However, the concept may be extended to other MSD schemes as well, such as RoLP and DT-CWT.

1) LPT+CS Based Fusion: In order to combine our CS rule with LPT, an extra step of band-pass filtering at the approximation level is needed to produce a corresponding detail level. This detail level is only used in the coefficient membership calculation but not involved in IMSD. Please note that there is only one subband at each decomposition level for LPT. The whole process of LPT+CS based fusion is summarized in Algorithm 1.

2) DWT+CS Based Fusion: Although it is possible to apply the same scheme for LPT-based fusion to DWT-based fusion, each detail level for DWT contains $2^D - 1$ subbands (D is the number of dimensions of the signal), which will result in significantly increased computational cost and poor consistency among subbands. Therefore, corresponding coefficients in different subbands at the same scale are evaluated together and the same membership is assigned to all of them. Hence, $A^n_{k,d,i}$ used in Equation (3) is substituted with the following:

$$\hat{A}^n_{k,d,i} = \max(A^n_{k,1,i}, \ldots, A^n_{k,2^D-1,i}). \tag{8}$$

The whole process of DWT+CS based fusion is summarized in Algorithm 2.

C. Color Fusion

In this section, we introduce an efficient color fusion scheme for the case of two monochrome source images utilizing the fusion result from the previous section. This color fusion scheme is inspired by the color opponency theory in physiology [40], which states that human perception of achromatic and chromatic colors occurs in three independent dimensions, *i.e.,* black-white (luminance), red-green, and yellow-blue. Contrast sensitivity in these three dimensions were studied by many researchers [44]–[46]. The contrast sensitivity function of luminance shows band-pass characteristics, while the contrast sensitivity functions of both red-green and yellow-blue show low-pass behavior. Therefore, luminance sensitivity is normally higher than chromatic sensitivity except at low spatial frequencies. Hence, the fused monochrome image, which provides combined information and good contrasts, should be assigned to the luminance channel to exploit luminance contrast. In addition, the color-fused image should also provide good contrasts in the red-green and yellow-blue channels in

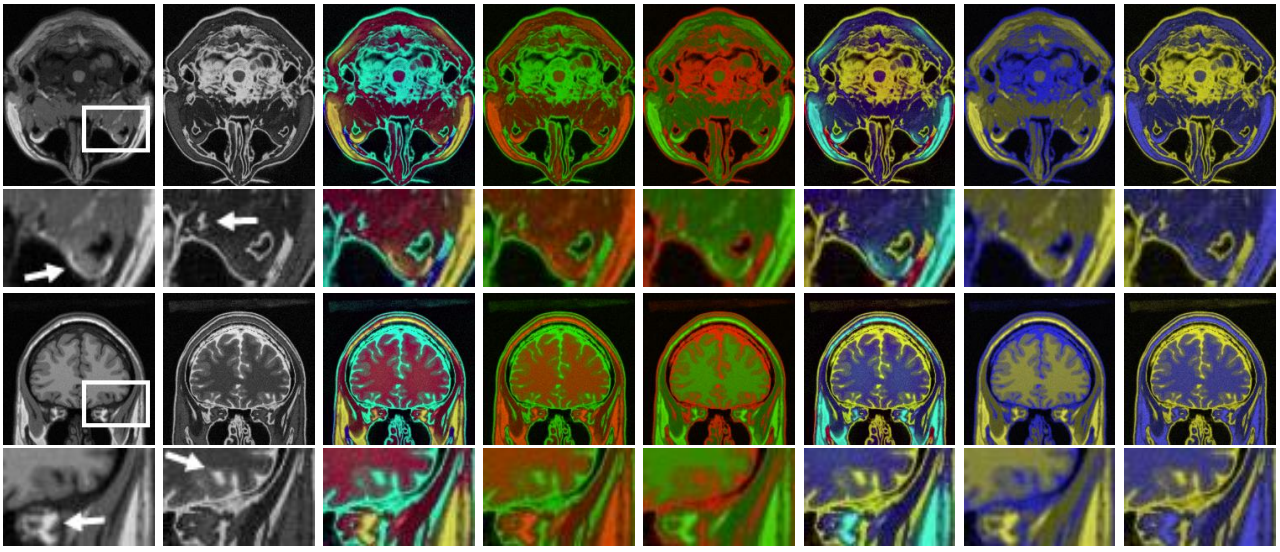

(a) (b) (c) (d) (e) (f) (g) (h)

Fig. 3. Comparison between our color fusion scheme and the overlaying scheme. The first row shows a slice in the axial direction from each volume. The second row shows slices in the coronal direction. Our scheme provides more image contrast, which makes the combined details more distinguishable, such as those indicated by the arrows in the insets. (a) T1W MRI slices; (b) T2W MRI slices; (c) Our color fusion results with $\bar{\mathbf{I}}_r^c = \mathbf{I}_1, \bar{\mathbf{I}}_b^c = \mathbf{I}_2$; (d) Overlaid images with $\bar{\mathbf{I}}_r^c = \mathbf{I}_1, \bar{\mathbf{I}}_g^c = \mathbf{I}_2$; (e) Overlaid images with $\bar{\mathbf{I}}_r^c = \mathbf{I}_2, \bar{\mathbf{I}}_g^c = \mathbf{I}_1$; (f) Our color fusion results with $\bar{\mathbf{I}}_r^c = \mathbf{I}_2, \bar{\mathbf{I}}_b^c = \mathbf{I}_1$; (g) Overlaid images with $\bar{\mathbf{I}}_r^c = \bar{\mathbf{I}}_g^c = \mathbf{I}_1, \bar{\mathbf{I}}_b^c = \mathbf{I}_2$; (h) Overlaid images with $\bar{\mathbf{I}}_r^c = \bar{\mathbf{I}}_g^c = \mathbf{I}_2, \bar{\mathbf{I}}_b^c = \mathbf{I}_1$.

order to fully exploit human color perception. To achieve this, we can consider red, green, yellow, and blue are arranged on a color circle as in [40], where the red-green axis is orthogonal to the yellow-blue axis and color (actually its hue) transits smoothly from one to another in each quadrant. Then, in order to maximize color contrast/dissimilarity between an object and its surroundings in the color-fused image, their hues should come from two opposite quadrants or at least from two orthogonal hues on the color circle. With these considerations, we have developed the following scheme.

Let $\mathbf{I}_1$ and $\mathbf{I}_2$ denote the two source images and $\bar{\mathbf{I}}$ the monochrome fused image. $\bar{\mathbf{I}}$ is considered as the luminance image of the color-fused image $\bar{\mathbf{I}}^c$. Therefore, if we consider the YUV color space, $\bar{\mathbf{I}}$ is the Y component. Let $\bar{\mathbf{I}}_r^c$, $\bar{\mathbf{I}}_g^c$, and $\bar{\mathbf{I}}_b^c$ denote the red, green, and blue color planes of $\bar{\mathbf{I}}^c$, respectively. The source images are assigned to the red and blue planes in the RGB color space (*i.e.,* $\bar{\mathbf{I}}_r^c = \mathbf{I}_1, \bar{\mathbf{I}}_b^c = \mathbf{I}_2$ or $\bar{\mathbf{I}}_r^c = \mathbf{I}_2, \bar{\mathbf{I}}_b^c = \mathbf{I}_1$), and the green plane is derived by reversing the calculation of the Y component from the RGB color space:

$$\bar{\mathbf{I}}_g^c = (\bar{\mathbf{I}} - 0.299\bar{\mathbf{I}}_r^c - 0.114\bar{\mathbf{I}}_b^c)/0.587. \quad (9)$$

This scheme provides more contrast enhancement than the overlaying schemes, because it fully utilizes color opponency in human perception. A visual comparison of slices from two directions is provided in Figure 3. An inset is given below each slice, which clearly shows the improved contrast using our scheme, as indicated by the white arrows.

IV. Experimental Results

The performance of the proposed cross-scale fusion rule was evaluated on volumetric image fusion of T1W and T2W MRI scans using both synthetic (Section IV-B) and real data (Section IV-C). There are three basic types of structural MRI: T1W, T2W, and proton density-weighted (PDW). Here, we only consider the fusion of T1W and T2W scans, because this combination produces more informative fusion result than the other two combinations (*i.e.,* T1W+PDW and T2W+PDW) as shown in [47].

In our experiments, only CBA was employed as the activity-level measurement. This is because: 1) As evaluated in [33], CBA is one of the measures that give the best performance; 2) Our CS rule has no restriction on the activity level and employing the same activity-level measure in all methods gives a fair comparison between our CS rule and existing fusion rules. To compare the performance of our CS rule with existing rules, three grouping schemes were considered: NG, CBSG, and MG; two combining schemes for the approximation level (APX) were considered: AVG and WA; one combining scheme for the detail levels (DET) is considered: CM; three verification schemes were considered: NV, WBV, and CBV. Please note that only CM can be used for the approximation level when MG is used due to the nature of MG and that CBV can only be used with CBSG due to the nature of CBSG. For WA and WBV, we took a $5 \times 5 \times 5$ neighborhood/window. We used the suggested threshold value of 0.85 in WA [25]. The two suggested threshold values of 0.2 and 0.5 in [28] were used in CBV. Two MSD schemes were considered: LPT and DWT. For DWT, we used the wavelet package provided by [48] and employed the 2-band orthogonal near-symmetric filters with $K = 2, L = 6$ [49]. 5-level decomposition was applied in LPT and 4-level decomposition was applied in DWT. Please note that the approximation level in an N-level LPT has the same size as that in an $(N-1)$-level DWT. All methods were implemented in Matlab, run on the same computer, and applied directly to the 3D volumes other than 2D slices. Two free parameters (γ and σ) are in our CS

TABLE I
OBJECTIVE EVALUATION RESULTS ON LPT-BASED FUSION OF SYNTHETIC AND REAL DATA USING $Q^{AB/F}$ METRIC.

Grouping	CS	NG				CBSG						MG	
APX combining	CS	AVG		WA		AVG			WA			CM	
DET combining	CS	CM		CM		CM			CM			CM	
Verification	CS	NV	WBV	NV	WBV	NV	WBV	CBV	NV	WBV	CBV	NV	WBV
Synthetic normal	**0.7727**	0.6566	0.7022	0.6529	0.6965	0.6532	0.6928	0.5982	0.6492	0.6871	0.5974	0.6609	0.6675
Synthetic lesion	**0.7810**	0.6221	0.6867	0.6120	0.6729	0.6265	0.6853	0.5697	0.6163	0.6718	0.5683	0.6763	0.6837
Real #1002	**0.6662**	0.5661	0.6325	0.5656	0.6321	0.5615	0.6181	0.4758	0.5611	0.6177	0.4755	0.6092	0.6149
Real #1037	0.6301	0.5395	0.5941	0.5399	0.5944	0.54	0.5840	0.4601	0.5404	0.5898	0.4605	0.6243	**0.6305**
Real #1215	**0.6803**	0.5835	0.6521	0.5833	0.6520	0.5783	0.6313	0.4843	0.5781	0.6311	0.4843	0.6169	0.6233
Real #1344	**0.6338**	0.5115	0.5874	0.5103	0.5863	0.5117	0.5726	0.4365	0.5105	0.5714	0.4352	0.5748	0.5807
Real #1372	**0.6560**	0.5627	0.6144	0.5630	0.6147	0.5622	0.6123	0.4765	0.5626	0.6126	0.4771	0.6261	0.6313

TABLE II
OBJECTIVE EVALUATION RESULTS ON DWT-BASED FUSION OF SYNTHETIC AND REAL DATA USING $Q^{AB/F}$ METRIC.

Grouping	CS	NG				CBSG						MG	
APX combining	CS	AVG		WA		AVG			WA			CM	
DET combining	CS	CM		CM		CM			CM			CM	
Verification	CS	NV	WBV	NV	WBV	NV	WBV	CBV	NV	WBV	CBV	NV	WBV
Synthetic normal	**0.7217**	0.5610	0.6719	0.5481	0.6556	0.5579	0.6405	0.4840	0.5443	0.6248	0.4792	0.6115	0.6220
Synthetic lesion	**0.7195**	0.5343	0.6540	0.5133	0.6213	0.5480	0.6217	0.4659	0.5246	0.5898	0.4528	0.6106	0.5834
Real #1002	**0.6140**	0.4950	0.4896	0.4942	0.4887	0.5144	0.5265	0.4110	0.5136	0.5255	0.4110	0.5828	0.5606
Real #1037	0.5578	0.4688	0.4478	0.4690	0.4481	0.4802	0.5180	0.3917	0.4804	0.5183	0.3917	**0.5824**	0.5513
Real #1215	**0.6338**	0.5081	0.5314	0.5073	0.5309	0.5285	0.5508	0.4211	0.5278	0.5502	0.4211	0.5944	0.5740
Real #1344	**0.5638**	0.4347	0.4489	0.4336	0.4475	0.4583	0.5056	0.3765	0.4571	0.5039	0.3761	0.5598	0.5386
Real #1372	0.5908	0.4955	0.4976	0.4959	0.4981	0.5085	0.5722	0.4090	0.5088	0.5730	0.4089	0.5991	**0.6010**

TABLE III
AVERAGE RANKINGS OF DIFFERENT FUSION RULES ON THE REAL DATA USING $Q^{AB/F}$ METRIC.

Grouping	CS	NG				CBSG						MG	
APX combining	CS	AVG		WA		AVG			WA			CM	
DET combining	CS	CM		CM		CM			CM			CM	
Verification	CS	NV	WBV	NV	WBV	NV	WBV	CBV	NV	WBV	CBV	NV	WBV
LPT-based	**1.02**	9.58	4.04	8.58	3.2	10.42	6.18	12.88	9.42	5.36	12.12	4.7	3.5
DWT-based	**1.58**	9.82	9.76	8.98	8.96	7.12	4.84	12.76	6.34	4.16	12.24	1.66	2.78

rule. Taking $\gamma = 10, \sigma = 1$ produced the best results in the experiments on the synthetic data, and therefore, we also used these values in the experiments on the real data.

A. Objective Evaluation Metric

The objective metric $Q^{AB/F}$ [50] was employed in the evaluation of the fusion quality. This metric does not require an ideal composite image as a reference image, which is difficult to get in practical cases. $Q^{AB/F}$ has been proven to correspond well with subjective tests among different metrics [51] and widely used in the image fusion community [30], [52]. $Q^{AB/F}$ measures the amount of edge information correctly transferred from source images to the fused image; and a $Q^{AB/F}$ score is within the range $[0, 1]$, where a higher score indicates better fusion result.

B. Evaluation Using Synthetic Data

Our CS rule was evaluated on two sets of realistic simulated 3D MRI brain images from BrainWeb [53], which are constructed based on real scans. The scans in each set are spatially registered due to the nature of the simulation. Each scan has $181 \times 217 \times 181$ voxels with 12-bit precision, and the size of each voxel is 1 mm^3. One set contains images of a normal brain, and the other contains images of a brain with moderate multiple sclerosis lesions. The objective evaluation results for LPT- and DWT-based fusion are summarized in Tables I and II (first two rows), respectively. Our CS rule has the best performance in transferring edge information on both datasets as indicated by the highest $Q^{AB/F}$ scores. Between LPT and DWT, LPT gives better performance for these datasets. With the other settings the same, WBV gives better performance than NV and CBV; and AVG gives better performance than WA. Therefore, for brevity, only NG+AVG+CM+WBV, CBSG+AVG+CM+WBV, and MG+CM+CM+WBV are visually compared with our CS rule on the lesion dataset in Figure 4. Only one slice along the axial direction from each volume is displayed and these slices are normalized to 8-bit precision for viewing. Please note that when viewed using a medical image visualization software (*e.g.,* VolView), the voxel values are usually not normalized, but instead, the display range of the voxel values and the image contrast can be interactively adjusted via the window/level setting. Compared to other fusion rules, our CS rule not only correctly combined information with high consistency with the source images, but also provided good local contrasts (*e.g.,* between ventricles, grey matter and white matter). As shown in the insets below each slice (refer to the regions pointed by the white arrows), our CS rule successfully eliminated the blocking artifacts shown in MG when coupled with LPT and the aliasing artifacts in NV, CBSG, and MG when coupled with DWT.

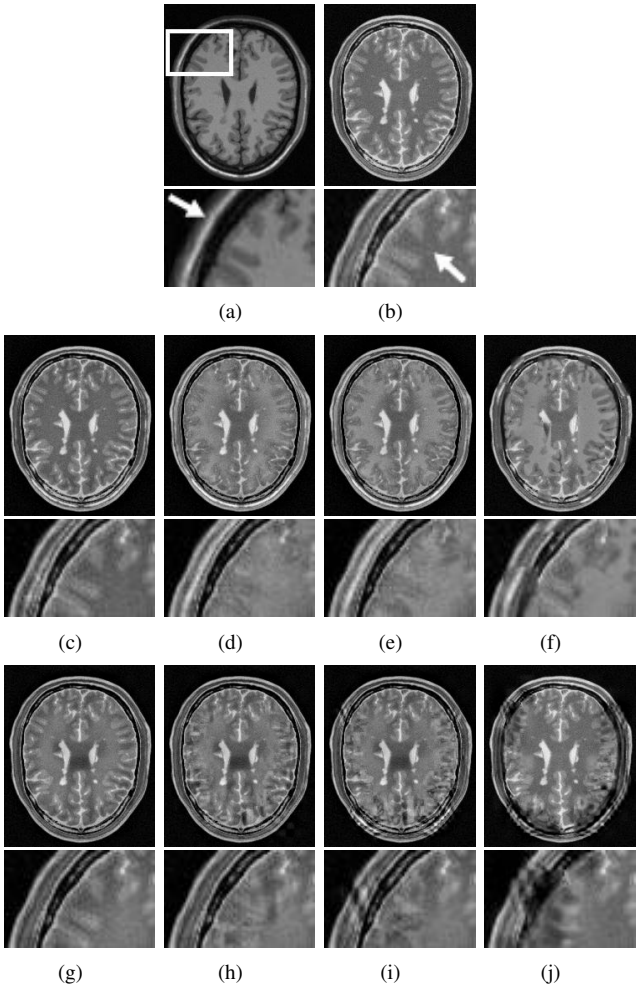

Fig. 4. Comparison of different fusion rules using synthetic MRI brain images. Our CS rule provides better reproduction of local details. (a) T1W MRI image; (b) T2W MRI image; (c) LPT+CS; (d) LPT+NG+AVG+CM+WBV; (e) LPT+CBSG+AVG+CM+WBV; (f) LPT+MG+CM+CM+WBV; (g) DWT+CS; (h) DWT+NG+AVG+CM+WBV; (i) DWT+CBSG+AVG+CM+WBV; (j) DWT+MG+CM+CM+WBV.

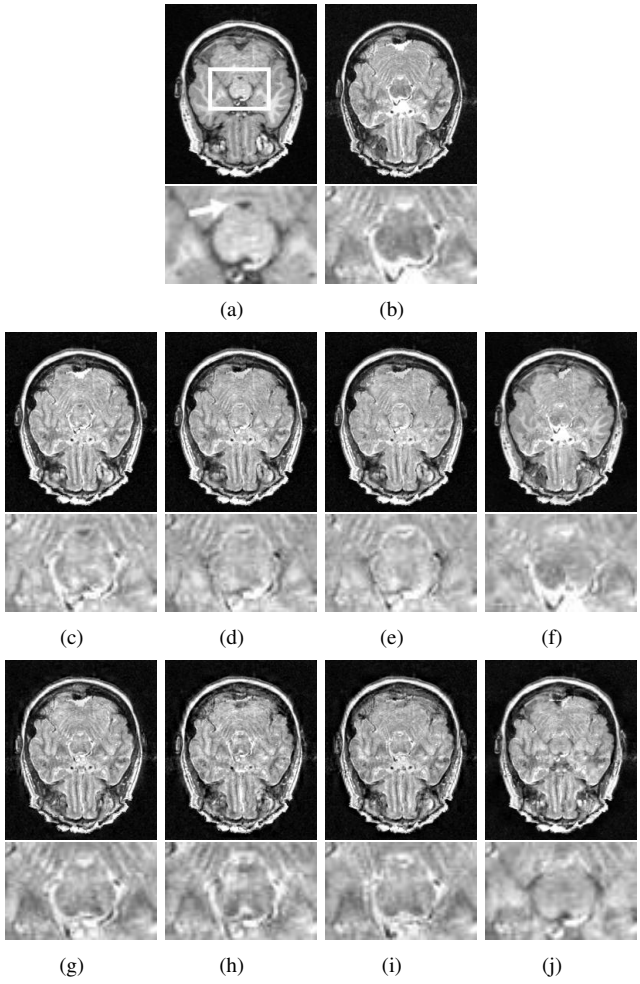

Fig. 5. Comparison of different fusion rules using real dataset #1002. Our CS rule provides better reproduction of local details with better consistencies at region boundaries. (a) T1W MRI image; (b) T2W MRI image; (c) LPT+CS; (d) LPT+NG+AVG+CM+WBV; (e) LPT+CBSG+AVG+CM+WBV; (f) LPT+MG+CM+CM+WBV; (g) DWT+CS; (h) DWT+NG+AVG+CM+WBV; (i) DWT+CBSG+AVG+CM+WBV; (j) DWT+MG+CM+CM+NV.

C. Evaluation Using Real Data

We also tested our method on fifty real datasets of normal brains randomly selected from the NIH Pediatric MRI Data Repository [54]. Each dataset contains stereotaxically registered MRI scans of the same subject. We used the T1W and T2W scans in each dataset to evaluate the proposed fusion method. Each scan has $197 \times 233 \times 189$ voxels with 32-bit precision, and the size of each voxel is 1 mm^3. The objective evaluation results on five representative datasets for LPT- and DWT-based fusion are summarized in Tables I and II (last five rows), respectively. According to the $Q^{AB/F}$ scores, the fusion rules are ranked from 1 (best) to 13 (worst) for each dataset. The average rankings on all the 50 datasets are presented in Table III. Our CS rule has the best performance in transferring edge information on the average. With the other settings the same, AVG and WA have very close performance for both LPT and DWT; WBV has better performance than NV and CBV for LPT; NV and WBV have similar performance for DWT+NG; WBV has better performance than NV and CBV for DWT+CBSG; and NV has better performance than WBV for DWT+MG. The results on a representative case (dataset #1002) are visually compared in Figure 5. For brevity, only NG+AVG+CM+WBV, CBSG+AVG+CM+WBV, LPT+MG+CM+CM+WBV, and DWT+MG+CM+CM+NV are visually compared with our CS rule. The displayed slices are normalized to 8-bit precision for viewing. As shown in the insets (refer to the cerebellum and the regions around the fourth ventricle as indicated by the white arrow), our CS rule produced better consistencies at region boundaries and gave better local details and contrasts. It can be seen from Table III that MG+CM+CM+NV has performance close to our CS rule in DWT-based fusion on the average, and MG has slightly better performance on some datasets as shown in Tables I and II. However, this interpretation is based on the $Q^{AB/F}$ scores, which only considers edge information. Without correctly transferred neighborhood information, the fusion results (even with higher $Q^{AB/F}$ scores) tend to contain artifacts. These artifacts will impair further analysis either by a radiologist or by image processing software. Our CS rule

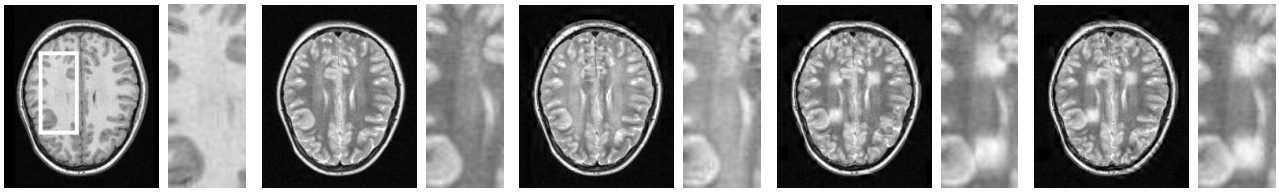

(a) (b) (c) (d) (e)

Fig. 6. Comparison of different fusion rules using real dataset #1372. Our CS rule provides better neighborhood consistencies. The artifacts produced by the MG rule in the white matter do not appear in the result by our CS rule. (a) T1W MRI image; (b) T2W MRI image; (c) DWT+CS; (d) DWT+MG+CM+CM+NV; (e) DWT+MG+CM+CM+WBV.

effectively minimizes the occurrence of such artifacts. An example is given in Figure 6. Our CS rule produced better neighborhood consistencies in the white matter.

V. Conclusion and Future Work

In this paper, we proposed a cross-scale fusion rule. Our fusion rule selects an optimal set of coefficients for each decomposition level, and guarantees intra- and inter-scale consistencies. Experiments on volumetric medical image fusion demonstrated the effectiveness of our cross-scale fusion rule, which produced fused images with higher quality than existing rules. An efficient color fusion scheme effectively utilizing monochrome fusion result was also proposed. In future work, we will extend our cross-scale rule to fusion of images acquired in other modalities, *e.g.,* CT and diffusion tensor MRI. We will also explore the possibility of combining our fusion rule with other MSD schemes.

References

[1] J. B. A. Maintz and M. A. Viergever, "A survey of medical image registration," *Med. Image Anal.*, vol. 2, no. 1, pp. 1–36, 1998.

[2] V. D. Calhoun and T. Adali, "Feature-based fusion of medical imaging data," *IEEE Trans. Info. Tech. Biomed.*, vol. 13, no. 5, pp. 711–720, 2009.

[3] M. Mahvash, R. König, H. Urbach, J. von Ortzen, B. Meyer, J. Schramm, and C. Schaller, "FLAIR-/T1-/T2-co-registration for image-guided diagnostic and resective epilepsy surgery," *Neurosurgery*, vol. 58, no. 1, pp. 69–75, 2006.

[4] C. R. Traynor, G. J. Barker, W. R. Crum, S. C. R. Williams, and M. P. Richardson, "Segmentation of the thalamus in MRI based on T1 and T2," *NeuroImage*, vol. 56, no. 3, pp. 939–950, 2011.

[5] A. Polo, F. Cattani, A. Vavassori, D. Origgi, G. Villa, H. Marsiglia, M. Bellomi, G. Tosi, O. de Cobelli, and R. Orecchia, "MR and CT image fusion for postimplant analysis in permanent prostate seed implants," *Int. J. Radiation Oncology Biol. Phys.*, vol. 60, no. 5, pp. 1572–1579, 2004.

[6] A. Boss, S. Bisdas, A. Kolb, M. Hofmann, U. Ernemann, C. D. Claussen, C. Pfannenberg, B. J. Pichler, M. Reimold, and L. Stegger, "Hybrid PET/MRI of intracranial masses: Initial experiences and comparison to PET/CT," *J. Nucl. Med.*, vol. 51, no. 8, pp. 1198–1205, 2010.

[7] B. Solaiman, R. Debon, F. Pipelier, J.-M. Cauvin, and C. Roux, "Information fusion: Application to data and model fusion for ultrasound image segmentation," *IEEE Trans. Biomed. Eng.*, vol. 46, no. 10, pp. 1171–1175, 1999.

[8] M. J. Gooding, K. Rajpoot, S. Mitchell, P. Chamberlain, S. H. Kennedy, and J. A. Noble, "Investigation into the fusion of multiple 4-D fetal echocardiography images to improve image quality," *Ultrasound in Med. & Biol.*, vol. 36, no. 6, pp. 957–966, 2010.

[9] R. S. Blum, Z. Xue, and Z. Zhang, *Multi-Sensor Image Fusion and Its Applications*. CRC Press, 2005, ch. An overview of image fusion, pp. 1–36.

[10] A. A. Goshtasby and S. Nikolov, "Image fusion: Advances in the state of the art," *Inf. Fusion*, vol. 8, no. 2, pp. 114–118, 2007.

[11] Z. Zhang and R. S. Blum, "A categorization of multiscale-decomposition-based image fusion schemes with a performance study for a digital camera application," *Proc. IEEE*, vol. 87, no. 8, pp. 1315–1326, 1999.

[12] C. S. Pattichis, M. S. Pattichis, and E. Micheli-Tzanakou, "Medical imaging fusion applications: An overview," in *Proc. 35th Asilomar Conf. Signals, Systems and Computers*, vol. 2, 2001, pp. 1263–1267.

[13] A. Jackson, N. A. Thacker, and S. M. Stivaros, *Image Processing in Radiology: Current Applications*. Springer, 2007, ch. 3D image fusion, pp. 101–122.

[14] F. L. Giesel, A. Mehndiratta, J. Locklin, M. J. McAuliffe, S. White, P. L. Choyke, M. V. Knopp, B. J. Wood, U. Haberkorn, and H. von Tengg-Kobligk, "Image fusion using CT, MRI and PET for treatment planning, navigation and follow up in percutaneous RFA," *Exp. Oncol.*, vol. 31, no. 2, pp. 106–114, 2009.

[15] B. C. Porter, D. J. Rubens, J. G. Strang, J. Smith, S. Totterman, and K. J. Parker, "Three-dimensional registration and fusion of ultrasound and MRI using major vessels as fiducial markers," *IEEE Trans. Med. Imag.*, vol. 20, no. 4, pp. 354–359, 2001.

[16] M. I. Smith and J. P. Heather, "A review of image fusion technology in 2005," in *Proc. SPIE*, vol. 5782, 2005, pp. 29–45.

[17] L. Wald, "Some terms of reference in data fusion," *IEEE Trans. Geoscience and Remote Sensing*, vol. 37, no. 3, pp. 1190–1193, 1999.

[18] G. Piella, "A general framework for multiresolution image fusion: from pixels to regions," *Inf. Fusion*, vol. 4, no. 4, pp. 259–280, 2003.

[19] M. Aguilar and J. R. New, "Fusion of multi-modality volumetric medical imagery," in *Proc. Int. Conf. Inf. Fusion*, vol. 2, 2002, pp. 1206–1212.

[20] D. L. Hall and J. Llinas, "An introduction to multisensor data fusion," *Proc. IEEE*, vol. 85, no. 1, pp. 6–23, 1997.

[21] P. Burt and E. H. Adelson, "The Laplacian pyramid as a compact image code," *IEEE Trans. Comm.*, vol. 31, no. 4, pp. 532–540, 1983.

[22] P. Burt, *Multiresolution Image Processing and Analysis*. Springer-Verlag, 1984, ch. The pyramid as a structure for efficient computation, pp. 6–35.

[23] A. Toet, "Hierarchical image fusion," *Mach. Vision Appl.*, vol. 3, no. 1, pp. 1–11, 1990.

[24] S. Winkler, "Vision models and quality metrics for image processing applications," Ph.D. dissertation, EPFL, 2000.

[25] P. J. Burt and R. J. Kolczynski, "Enhanced image capture through fusion," in *Proc. 4th Int. Conf. Comput. Vis.*, 1993, pp. 173–182.

[26] V. Petrović and C. Xydeas, "Gradient-based multiresolution image fusion," *IEEE Trans. Image Process.*, vol. 13, no. 2, pp. 228–237, 2004.

[27] S. G. Mallat, "A theory for multiresolution signal decomposition: The wavelet representation," *IEEE Trans. Pattern Anal. Mach. Intell.*, vol. 11, no. 7, pp. 674–693, 1989.

[28] H. Li, B. S. Manjunath, and S. K. Mitra, "Multisensor image fusion using the wavelet transform," *Graph. Models Image Process.*, vol. 57, no. 3, pp. 235–245, 1995.

[29] R. Singh, M. Vatsa, and A. Noore, "Multimodal medical image fusion using redundant discrete wavelet transform," in *Proc. 7th Int. Conf. Advances in Pattern Recognit.*, 2009, pp. 232–235.

[30] S. Li, B. Yang, and J. Hu, "Performance comparison of different multi-resolution transforms for image fusion," *Inf. Fusion*, vol. 12, no. 2, pp. 74–84, 2011.

[31] J. E. Fowler, "The redundant discrete wavelet transform and additive noise," *IEEE Signal Process. Lett.*, vol. 12, no. 9, pp. 629–632, 2005.

[32] I. W. Selesnick, R. G. Baraniuk, and N. C. Kingsbury, "The dual-tree complex wavelet transform," *IEEE Signal Process. Magazine*, vol. 22, no. 6, pp. 123–151, 2005.

[33] G. Pajares and J. M. de la Cruz, "A wavelet-based image fusion tutorial," *Pattern Recognit.*, vol. 37, no. 9, pp. 1855–1872, 2004.

[34] J. J. Lewis, R. J. O'Callaghan, S. G. Nikolov, D. R. Bull, and N. Canagarajah, "Pixel- and region-based image fusion with complex wavelets," *Inf. Fusion*, vol. 8, no. 2, pp. 119–130, 2007.
[35] V. Petrović and C. Xydeas, "Cross-band pixel selection in multiresolution image fusion," in *Proc. SPIE*, vol. 3719, 1999, pp. 319–326.
[36] Z. Zhang and R. S. Blum, "Region-based image fusion scheme for concealed weapon detection," in *Proc. Ann. Conf. Inf. Sciences and Systems*, 1997, pp. 168–173.
[37] K. Rajpoot, J. A. Noble, V. Grau, C. Szmigielski, and H. Becher, "Multiview RT3D echocardiography image fusion," in *Proc. Int. Conf. Functional Imaging and Modeling of the Heart*, vol. 5528, 2009, pp. 134–143.
[38] Z. Wang and Y. Ma, "Medical image fusion using m-PCNN," *Inf. Fusion*, vol. 9, no. 2, pp. 176–185, 2008.
[39] Y. Yang, D. S. Park, S. Huang, and N. Rao, "Medical image fusion via an effective wavelet-based approach," *EURASIP J. Advances in Signal Process.*, vol. 2010, no. 579341, pp. 1–13, 2010.
[40] E. Hering, *Outlines of a Theory of the Light Sense*. Harvard University Press, 1964, ch. The natural color system, pp. 25–65.
[41] C. Wang and Z. Ye, "First-order fusion of volumetric medical imagery," *IEE Proc., Vis. Image Process.*, vol. 153, no. 2, pp. 191–198, 2006.
[42] R. Shams, P. Sadeghi, R. Kennedy, and R. Hartley, "A survey of medical image registration on multicore and the GPU," *IEEE Signal Process. Magazine*, vol. 27, no. 2, pp. 50–60, 2010.
[43] R. Shen, I. Cheng, J. Shi, and A. Basu, "Generalized random walks for fusion of multi-exposure images," *IEEE Trans. Image Process.*, vol. 20, no. 12, pp. 3634–3646, 2011.
[44] K. T. Mullen, "The contrast sensitivity of human colour vision to red-green and blue-yellow chromatic gratings," *J. Physiol.*, vol. 359, pp. 381–400, 1985.
[45] J. M. Rovamo, M. I. Kankaanpaa, and H. Kukkonen, "Modelling spatial contrast sensitivity functions for chromatic and luminance-modulated gratings," *Vision Res.*, vol. 39, no. 14, pp. 2387–2398, 1999.
[46] J. E. Thornton and E. N. Pugh, "Red/green color opponency at detection threshold," *Science*, vol. 219, no. 4581, pp. 191–193, 1983.
[47] Y. Zheng, A. S. Elmaghraby, and H. Frigui, "Three-band MRI image fusion utilizing the wavelet-based method optimized with two quantitative fusion metrics," in *Proc. SPIE*, vol. 6144, 2006, pp. 61 440R–1–61 440R–12.
[48] S. Cai, K. Li, and I. Selesnick, "Wavelet software at Polytechnic University, Brooklyn, NY," http://eeweb.poly.edu/iselesni/WaveletSoftware/, accessed April 2010.
[49] A. F. Abdelnour and I. W. Selesnick, "Design of 2-band orthogonal near-symmetric CQF," in *Proc. IEEE Int. Conf. Acoust., Speech, and Signal Process.*, vol. 6, 2001, pp. 3693–3696.
[50] C. S. Xydeas and V. Petrović, "Objective image fusion performance measure," *Electron. Lett.*, vol. 36, no. 4, pp. 308–309, 2000.
[51] V. Petrović, "Subjective tests for image fusion evaluation and objective metric validation," *Inf. Fusion*, vol. 8, no. 2, pp. 208–216, 2007.
[52] Z. Liu, E. Blasch, Z. Xue, J. Zhao, R. Laganiere, and W. Wu, "Objective assessment of multiresolution fusion algorithms for context enhancement in night vision: A comparative study," *IEEE Trans. Pattern Anal. Mach. Intell.*, vol. 34, no. 1, pp. 94–109, 2011.
[53] R. K.-S. Kwan, A. C. Evans, and G. B. Pike, "MRI simulation-based evaluation of image-processing and classification methods," *IEEE Trans. Med. Imag.*, vol. 18, no. 11, pp. 1085–1097, 1999, http://www.bic.mni.mcgill.ca/brainweb/.
[54] Brain Development Cooperative Group and A. C. Evans, "The NIH MRI study of normal brain development," *NeuroImage*, vol. 30, no. 1, pp. 184–202, 2006, https://nihpd.crbs.ucsd.edu/nihpd/info/.